NANO LETTERS

Letter

pubs.acs.org/NanoLett

Ultralow Self-Doping in Two-dimensional Hybrid Perovskite Single Crystals

Wei Peng,[†,¶,Δ] Jun Yin,[†] Kang-Ting Ho,[‡] Olivier Ouellette,[§] Michele De Bastiani,[†] Banavoth Murali,[†,#] Omar El Tall,[⊥] Chao Shen,[‡] Xiaohe Miao,[∥] Jun Pan,[†] Erkki Alarousu,[†] Jr-Hau He,[‡] Boon S. Ooi,[‡] Omar F. Mohammed,[†] Edward Sargent,[§] and Osman M. Bakr*[,†,¶,Δ]

[†]Division of Physical Sciences and Engineering, King Abdullah University of Science and Technology (KAUST), Thuwal 23955-6900, Saudi Arabia

[¶]KAUST Solar Center, King Abdullah University of Science and Technology (KAUST), Thuwal 23955-6900, Saudi Arabia

[Δ]KAUST Catalysis Center, King Abdullah University of Science and Technology (KAUST), Thuwal 23955-6900, Saudi Arabia

[‡]Division of Computer, Electrical and Mathematical Sciences and Engineering, King Abdullah University of Science and Technology (KAUST), Thuwal 23955-6900, Saudi Arabia

[⊥]Analytical Core Lab, King Abdullah University of Science and Technology (KAUST), Thuwal 23955-6900, Saudi Arabia

[∥]Imaging and Characterization Core Lab, King Abdullah University of Science and Technology (KAUST), Thuwal 23955-6900, Saudi Arabia

[§]Department of Electrical and Computer Engineering, University of Toronto, 10 King's College Road, Toronto, Ontario M5S 3G4, Canada

Supporting Information

ABSTRACT: Unintentional self-doping in semiconductors through shallow defects is detrimental to optoelectronic device performance. It adversely affects junction properties and it introduces electronic noise. This is especially acute for solution-processed semiconductors, including hybrid perovskites, which are usually high in defects due to rapid crystallization. Here, we uncover extremely low self-doping concentrations in single crystals of the two-dimensional perovskites $(C_6H_5C_2H_4NH_3)_2PbI_4{\cdot}(CH_3NH_3PbI_3)_{n-1}$ (n = 1, 2, and 3), over three orders of magnitude lower than those of typical three-dimensional hybrid perovskites, by analyzing their conductivity behavior. We propose that crystallization of hybrid perovskites containing large organic cations suppresses defect formation and thus favors a low self-doping level. To exemplify the benefits of this effect, we demonstrate extraordinarily high light-detectivity (10^{13} Jones) in $(C_6H_5C_2H_4NH_3)_2PbI_4{\cdot}(CH_3NH_3PbI_3)_{n-1}$ photoconductors due to the reduced electronic noise, which makes them particularly attractive for the detection of weak light signals. Furthermore, the low self-doping concentration reduces the equilibrium charge carrier concentration in $(C_6H_5C_2H_4NH_3)_2PbI_4{\cdot}(CH_3NH_3PbI_3)_{n-1}$, advantageous in the design of p−i−n heterojunction solar cells by optimizing band alignment and promoting carrier depletion in the intrinsic perovskite layer, thereby enhancing charge extraction.

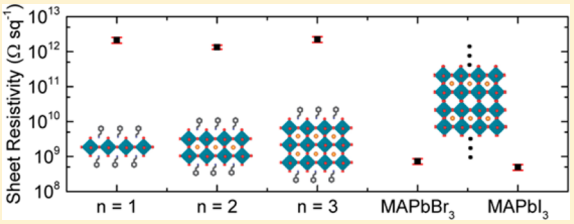

KEYWORDS: *Two-dimensional hybrid perovskites, shallow defects, unintentional self-doping, photodetector, single crystals*

The development of semiconductor technologies is intertwined with advancements in controlling semiconductor purity and doping, which are prerequisites for controlling the charge carrier density, Fermi level, density of in-gap states, and electronic noise.[1,2] Therefore, it is imperative to avoid unintentional doping that is caused by impurities and intrinsic defect states in order to achieve specific functionality, optimize device performance, and improve reproducibility. In solution-processed compound semiconductors, abundant intrinsic point defects including interstitials and vacancies with shallow energy levels are the main source of unintentional self-dopants. A typical example is hybrid perovskites, which are leading the pack of solution-processed semiconductors for optoelectronic devices, especially photovoltaics.[2−4] Specifically, in the commonly used p−i−n heterojunction device structure for perovskite solar cells, unintentional self-doping in the intrinsic perovskite layer has a profound impact on the band alignment and device working mechanism.[5,6] For example, a perovskite layer with a low equilibrium carrier concentration can be fully depleted in the heterojunction, thus benefiting photocarrier extraction.[5,7] In the field of photodetectors, which has seen a rapid upsurge in the use of hybrid perovskites as light-sensitive materials, unintentional doping increases electronic noise, which renders devices ineffective for detecting weak signals.[1,8,9] Therefore, a plausible

Received: April 9, 2017
Revised: June 10, 2017
Published: June 28, 2017

DOI: 10.1021/acs.nanolett.7b01475
Nano Lett. XXXX, XXX, XXX−XXX

way to reduce unintentional doping in hybrid perovskites is highly demanded for further advancement of their optoelectronic devices.

In the present work, we investigate self-doping in the single crystals of two-dimensional (2D) hybrid perovskites $PEA_2PbI_4\cdot(MAPbI_3)_{n-1}$ (PEA, phenethylammonium; MA, methylammonium; n = 1, 2, 3), which are essentially a periodic assembly of quantum-confined 2D hybrid perovskite sheets dielectrically separated by a spacer layer of PEA cations. We uncover extremely low self-doping concentrations in the 2D perovskite crystals, over three orders of magnitude lower than those of typical 3D perovskites ($MAPbI_3$ and $MAPbBr_3$), by examining their sheet conductivity behavior. We propose that the decrease in the self-doping level with the reduced crystal dimensionality is a consequence of a defect-suppressing crystallization process that is mediated by the large organic cation PEA. As a result of the low equilibrium carrier concentration, electronic noise in preliminary $PEA_2PbI_4\cdot(MAPbI_3)_{n-1}$ (n = 1, 2, 3) single crystal-based photoconductors markedly diminishes, giving rise to extraordinarily high light detectivity (10^{13} Jones). Furthermore, we predict this finding will lead to advancements in designing and optimizing perovskite solar cells, as optimized band alignment and increased charge extraction are expected.

Single crystals of $PEA_2PbI_4\cdot(MAPbI_3)_{n-1}$ (n = 1, 2, 3) were grown by cooling a saturated hydroiodic acid solution of precursors containing lead oxide, methylammonium iodide, and phenethylamine from above 80 °C to room temperature (see Experimental Methods for details), as reported before.[10] As-grown crystals show lamellar topography and increased darkening in color with higher n, as shown by the photographic images of the crystals in Figure S1 and Figure 1a inset.

To characterize the crystal structure, we first carried out X-ray diffraction (XRD) directly on the exfoliated crystal surface (Figure 1a). According to previous reports on the crystal structures of $PEA_2PbI_4\cdot(MAPbI_3)_{n-1}$ (n = 1, 2), the diffraction patterns of n = 1 and 2 samples can be indexed as shown in Figure 1a. The indexing confirms an in-plane orientation of the PbI_6 sheets along the exfoliated surface, as illustrated in Figure 1b. Powder XRD patterns of n = 1 and 2 samples are presented in Figure S2 and match with the calculated patterns from their reported single crystal structures.[11] Additionally, the lattice distance of the first diffraction peak in all three patterns were calculated to be 1.651, 2.281, and 2.812 nm for n = 1, 2, 3 samples, respectively, showing a stepwise increase of approximately 0.6 nm. This increment corresponds to the thickness of a single PbI_6 sheet, thus demonstrating the correct assignment of the structure for the n = 3 sample (Figure 1b).

The photoluminescence (PL) and absorption spectra of $PEA_2PbI_4\cdot(MAPbI_3)_{n-1}$ (n = 1, 2, 3) single crystals are presented in Figure 1c, showing a continuous bandgap decrement from 2.4 eV for n = 1, to 2.2 eV for n = 2, and further 2.0 eV for n = 3. The bandgap evolution resembles those of other 2D lead iodide perovskites since the electronic states of Pb and I dominate the band edge states.[10,12]

Simple in-plane devices based on the 2D perovskite single crystals were fabricated by thermally evaporating a pair of 60 nm-thick gold electrodes on freshly exfoliated crystals with a smooth surface (Figure 2a) through a metal shadow mask. The device structure is illustrated in the inset of Figure 2b. All the devices exhibit Ohmic conduction behavior with strikingly low dark currents on the level of 10^{-13} A (see Figure 2b). In contrast, devices of $MAPbI_3$ and $MAPbBr_3$ single crystals using the same

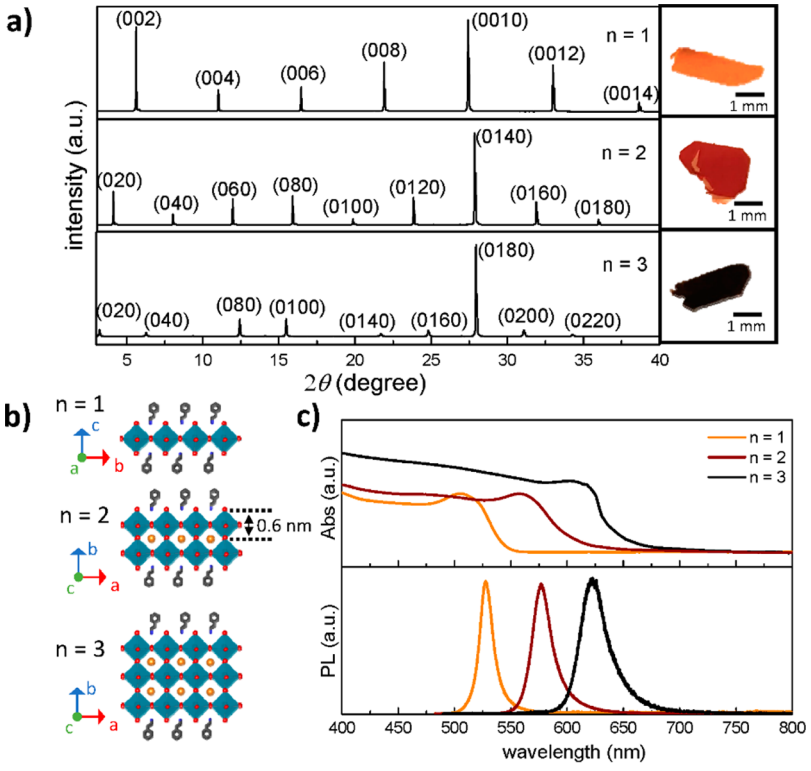

Figure 1. (a) XRD patterns by lock-in coupled θ–2θ scan of the freshly cleaved single crystals of $PEA_2PbI_4\cdot(MAPbI_3)_{n-1}$ (n = 1, 2, 3). The optical images of the freshly cleaved crystals are shown in the inset. (b) Schematic illustrations of the layered structure and the corresponding orientation of 2D perovskite crystals, showing that the thickness of a single perovskite sheet is approximately 0.6 nm. (c) PL spectra and the absorption spectra that were extracted by diffuse reflectance measurement of layered perovskite crystal powders.

DOI: 10.1021/acs.nanolett.7b01475
Nano Lett. XXXX, XXX, XXX−XXX

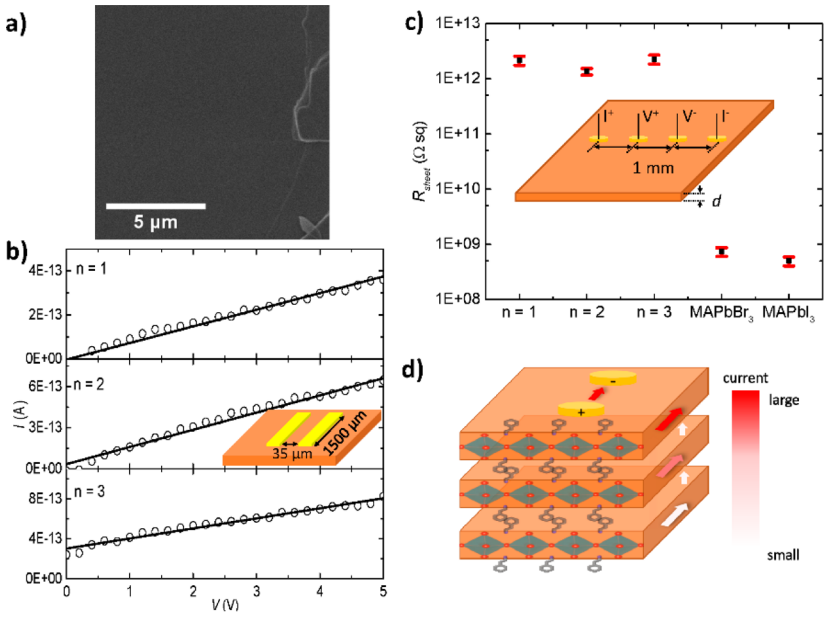

Figure 2. (a) SEM image of the freshly exfoliated 2D perovskite single crystal surface, showing a smooth surface. The image was captured at the edge of the crystal for better contrast. (b) Dark $I-V$ curves of $PEA_2PbI_4{\cdot}(MAPbI_3)_{n-1}$ (n = 1, 2, 3) single crystal devices with the device structure illustrated in the inset. (c) Measured sheet resistivity of $PEA_2PbI_4{\cdot}(MAPbI_3)_{n-1}$ (n = 1, 2, 3), $MAPbI_3$, and $MAPbBr_3$ in the dark using the four-point probe method as illustrated in the inset. The thickness, d, of the crystal is <10 μm for 2D perovskites, and 200 μm for 3D perovskites. (d) Schematic illustration of the confined charge carrier transport on the top of the 2D perovskite crystals.

device structure show five-orders-of-magnitude-larger dark currents (Figure S3). In order to precisely determine the resistivity, we carried out four-point probe measurement. Details of the measurement can be found in the Experimental Methods. The measured sheet resistivity, R_{sheet}, of the five crystals, $PEA_2PbI_4{\cdot}(MAPbI_3)_{n-1}$ (n = 1, 2, 3), $MAPbBr_3$, $MAPbI_3$, are plotted in Figure 2c. It is worth mentioning that the calculation in both cases, 2D and 3D perovskites, is based on an equation $R_{sheet} = \pi/\ln 2{\cdot}V/I$, where V is the measured bias drop between the two inner probes and I is the injected current of the outer electrodes.[13] This equation is derived for a model based on the assumption of infinite 2D sheets. The model is applicable to both types of perovskites considering that carrier transport in 2D perovskites is restricted to the surface (see the out-of-plane resistivity measurement in Figure S4), as illustrated in Figure 2d, while the 3D perovskite single crystals for the measurement were polished down to 200 μm, resulting in a correction factor close to unity within this model due to a probe distance of 1 mm.[13] We want to note here that all the conductivity measurements in this work were carried out by measuring the stable current/voltage output to avoid the possible contribution of ionic conduction to the measured conductivity. Thus, we can conclude a dramatic electrical conductivity difference between the 3D and 2D perovskites.

Electrical conductivity is an important and complex property of semiconductors, which contains information on the free carrier concentration and carrier mobilities.[14] The latter is further determined by the carrier scattering frequency during transport and electron/hole effective masses. Their relation is expressed as $\sigma = n_t e^2\tau/m^*$, where σ is the conductivity, n_t is the carrier density, μ is the electron/hole mobility, e is the elementary charge, τ is the carrier relaxation time, and m^* is electron/hole effective masses. Therefore, a difference in the conductivity can be attributed to differences in n_t, τ, and m^*. An over three-orders-of-magnitude difference in conductivity signifies a substantial variation of these three parameters when the dimension of the hybrid perovskites is reduced from 3D to 2D. Since these three factors are also correlated with other important properties of a semiconductor, such as defect densities and band structures, a closer examination of how their interplay contributes to the conductivity evolution from 3D to 2D perovskites is warranted.

Electron/hole effective masses are an intrinsic property of semiconductors, which are solely determined by the band structure. Therefore, we calculated the band structures of $PEA_2PbI_4{\cdot}(MAPbI_3)_{n-1}$ (Figure 3a) in accordance to their single crystal structures (Figure 3b) using the density functional theory (DFT). Calculation details can be found in Experimental Methods. As shown in Figure 3a, the calculated bandgaps are 2.31 eV (n = 1), 2.17 eV (n = 2), and 1.95 eV (n = 3), respectively, without considering spin−orbit coupling (SOC), in good agreement with experimental values deduced from the absorption spectra. Similar to $MAPbI_3$, the valence band maximum (VBM) of 2D hybrid perovskites consists of both Pb-6s and I-5p states, and conduction band minimum (CBM) is mainly composed of Pb-6p state (see the projected density of states in Figure S5). Once SOC effects were included in the band calculations, the bandgaps are considerably reduced to 1.43 eV (n = 1), 1.20 (n = 2), and 0.91 eV (n = 3) due to band splitting; however, band curvatures are almost unchanged and so are the effective masses. This calculation is consistent with previous reports.[12] The extracted values of electron/hole effective mass ($m^*_{e/h}$) along Γ−F direction are 0.278/0.604, 0.198/0.391, and 0.214/0.232 for n = 1, 2, 3, respectively. Although the charge carrier transport is limited in the 2D perovskite layer, the balanced hole and electron effective masses of 2D perovskites are comparable to those of 3D $MAPbI_3$ (see Figure S5 and Table S1), which was also pointed out in recent studies.[12] These findings suggest that effective masses can be ruled out as a major contribution to the conductivity difference between 2D and 3D perovskites.

The second factor to be investigated is the relaxation time τ, which is defined by the average free time-of-flight of a carrier between two scattering events. Among various scattering sources,

DOI: 10.1021/acs.nanolett.7b01475
Nano Lett. XXXX, XXX, XXX−XXX

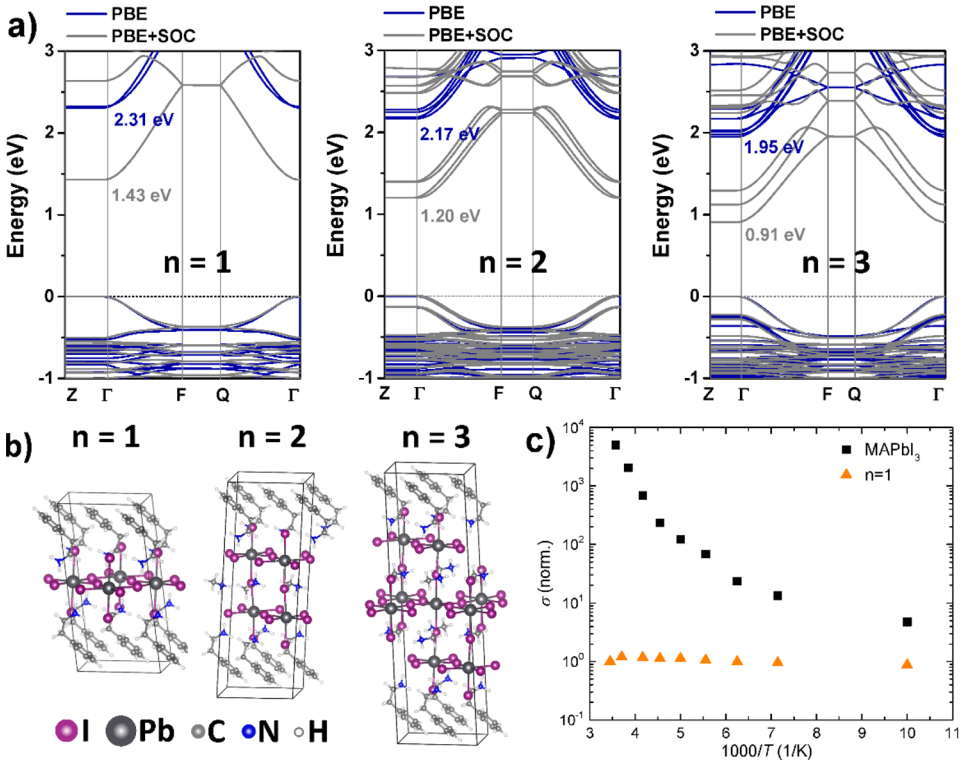

Figure 3. (a) Calculated band structures of $PEA_2PbI_4{\cdot}(MAPbI_3)_{n-1}$ (n = 1, 2, 3) at GGA/PBE level without and with account of SOC. (b) Corresponding crystal structures for the band structure calculation in panel (a). (c) Temperature-dependent conductivity (normalized) of $MAPbI_3$ and PEA_2PbI_4 single crystals.

ionized impurities and phonons are usually the major scatters.[14] Furthermore, in the context of hybrid perovskite single crystals that are absent of intentional doping, and at room temperature where we carried out the resistivity measurements, acoustic phonon scattering was found to play the major role in limiting carrier mobilities.[15−17] Here, the scattering by longitudinal acoustic phonons was estimated by the deformation potential theory.[16,17] As shown in Table S1, for both 2D and 3D hybrid perovskites, the deformation potential, D, of electrons is larger than that of holes. Interestingly, the deformation potentials increase with increasing n, confirming that lowering the dimension of a hybrid system lowers the deformation energy.[18] Besides, the deformation potentials of both 3D and 2D perovskites are within the same order of magnitude, suggesting their comparable electron-acoustic phonon scattering strength according to the relation $\tau \propto 1/m^*D^2$.[19]

The above considerations on m^* and τ set comparable upper limits to the charge carrier mobilities of $MAPbI_3$ and $(PEA)_2PbI_4{\cdot}(MAPbI_3)_{n-1}$ (n = 1, 2, 3). Indeed, carrier mobilities in 2D perovskite thin films have been experimentally measured in thin film transistors and found to be comparable to those reported in $MAPbI_3$ thin films.[20,21] More recently, photophysical studies by Herz's group demonstrated that the effective charge carrier mobility of 2D perovskites was comparable (within the same order of magnitude) to that of 3D perovskites.[22,23] Therefore, we infer that the last factor, the free carrier concentration n_f, should be the main cause for the significant conductivity difference between 3D lead halide perovskites and $PEA_2PbI_4{\cdot}(MAPbI_3)_{n-1}$. The sources of free carriers under thermal equilibrium can be one of two types: intrinsic carriers from thermal excitation of electrons from VBM to CBM, and extrinsic carriers by thermal excitation of electrons from (to) extrinsic donors (acceptors). The generation of the latter requires less energy, i.e., lower temperatures, as the energy levels of dopants lie within the bandgap. In the context of hybrid perovskite single crystals, the major doping role is played by unintentionally introduced shallow defect states.[2,4] In order to ascertain the carrier sources in the single crystals under discussion, we first carried out a calculation on the temperature dependence of conductivity in semiconductors while assuming several sets of parameters including the dopant concentration N_d, the dopant activation energy E_a, and the bandgap E_g.[24] As shown in Figure S6, the $\ln \sigma - 1/T$ (T is temperature) curve of a semiconductor shows two distinct regimes: an intrinsic regime at high temperatures where intrinsic carriers dominate conduction and an extrinsic regime at low temperatures where extrinsic carriers dominate conduction. We should note here that the precise calculation of the free carrier concentration contributed by dopants at low temperatures is more complicated than what we show in the Supporting Information, but a reasonable trend of the conductivity evolution with the temperature is offered by this approximation.[24] From the high-temperature intrinsic regime, a linear fitting can be used to extract the bandgap according to $n_i \propto e^{-E_g/2kT}$ (n_i is the intrinsic carrier density, k is Boltzmann constant). In the low-temperature extrinsic regime, a factor of $T^{-3/2}$ that is contributed by the electron−phonon scattering effect on the carrier mobility becomes distinct, especially for a semiconductor with a small dopant activation energy (<0.1 eV). For a semiconductor with a small activation energy of the dopants, as the temperature decreases, its conductivity slowly increases at first due to the reduced electron−phonon scattering strength, and then gradually decrease as a result of $n_e \propto e^{-E_a/2kT}$ (n_e is the extrinsic carrier density), corresponding to a process of dopant freezing. For a semiconductor with dopants possessing relatively larger

DOI: 10.1021/acs.nanolett.7b01475
Nano Lett. XXXX, XXX, XXX−XXX

activation energies (≥0.1 eV), only a steep conductivity decrease process is observed because the exponential dependence of dopant freezing process on temperature dominates over the power law dependence of the electron−phonon scattering strength. Another noticeable characteristic of the temperature-dependent conductivity is that the onset temperature of the intrinsic regime for a semiconductor with a bandgap larger than 1.5 eV is usually much higher than room temperature. This characteristic suggests that in both the 3D and 2D perovskites the dominant carriers at room temperature probably originate extrinsically from dopants.

To verify the extrinsic nature of the carriers in the perovskites under study, we measured temperature-dependent conductivity of PEA_2PbI_4 and $MAPbI_3$ single crystals. As shown in Figure 3c, the conductivity of PEA_2PbI_4 varies slightly with the temperature decreasing from 300 K down to 100 K, exhibiting an initially slight increase followed by a gradual decrease process. These characteristics demonstrate the extrinsic nature of the dominant carriers in PEA_2PbI_4 under room temperature and further suggest their small dopant activation energy. In contrast, $MAPbI_3$ exhibits much steeper conductivity reduction with the temperature decreasing. By simply fitting the linear regimes in the plot of $\ln(\sigma^* T^{3/2}) - 1/T$ (Figure S6), the extracted slope can be used to estimate the dopant activation energy according to $\ln(\sigma^* T^{3/2}) \propto -E_a/2k^* 1/T$. As shown in Figure S6, E_a extracted for $MAPbI_3$ has a relatively broad distribution from approximately 0.26 eV down to 0.04 eV, while for PEA_2PbI_4 only a small value of 0.03 eV exists. Indeed, a supportive conclusion that the dominant shallow defects in $MAPbI_3$ single crystals distributing broadly within 0.25 eV relative to band edges was also obtained through temperature-dependent space-charge limited current analysis.[25] As we have confirmed the extrinsic nature of the charge carriers in the perovskites under study, we can conclude the gap of intrinsic dopant concentrations as the major cause of the significant conductivity difference between the 3D and 2D perovskites. Furthermore, since a considerably smaller proportion of the dopants in the 3D perovskites compared to those of the 2D perovskites can be ionized at room temperature due to the much larger dopant activation energies in the 3D perovskites, more than three orders of magnitude difference in their dopant concentration is expected so as to realize the conductivity difference of over three orders of magnitude (see the calculated temperature-dependent conductivity curves of two semiconductors with the same bandgap and the same dopant concentration but significantly different dopant activation energy in Figure S6).

Our conclusion on the critical role of self-dopant concentration in the conductivity of the 2D perovskites is corroborated with other experimental facts. One of them is the evolution of their conductivity with the crystal storage time (in ambient condition, 60% relative humidity). As shown in Figure 4a, the conductivity of PEA_2PbI_4 exhibits an approaching two-orders-of-magnitude increase during the first 10 days of storage and subsequently decreases to an even lower value than the initial after 30 days. This conductivity evolution can be related to the perovskite degradation process. XRD measurement confirms the formation of PbI_2 and PEA-related byproducts during storage (Figure S7). Both scanning electronic microscopy (SEM) and optical microscopy further reveal that the decomposition causes the smooth exfoliated crystal surface to degrade into a porous structure (Figures S8 and 4b). The decomposition should introduce considerable defects at the fracture boundaries. The shallow ones can act as dopants to contribute excess free carriers and increase conductivity.[4] However, as the decomposition extent deepens, insulating byproducts would block the conductive channels, resulting in the eventual conductivity drop. The whole process is illustrated in the inset of Figure 4a.

Two-dimensional perovskite thin films are expected to show a higher conductivity due to their increased defect densities compared to single crystals. As shown in Figure 4c, the spin-coated thin film of PEA_2PbI_4 with a (002) crystallographic orientation (see Figure S9, the same as its single crystal) exhibits two orders of magnitude larger dark current (on the level of 10^{-11} A) than single crystals. In the cases of $PEA_2PbI_4{\cdot}(MAPbI_3)_{n-1}$ (n = 2, 3) thin films, the situation is quite different since phase separation happens in the film deposition process. As clearly shown in Figure S10, XRD and PL spectroscopy confirm the formation of dominant PEA_2PbI_4 and $MAPbI_3$ phases.[26] Phase separation is possibly a result of the large solubility difference between PEAI and MAI. Consequently, these two films show even larger dark currents on the level of 10^{-8} A, which is the conductivity behavior of $MAPbI_3$ thin films (Figure S11).

Shallow defects have been known to cause $I-V$ hysteresis in hybrid perovskite-based optoelectronic devices.[27−29] In sharp contrast to the serious hysteresis observed in $MAPbI_3$ and $MAPbBr_3$ single crystal devices, all the fresh devices based on 2D perovskite single crystals showed no hysteresis (Figure S12). However, hysteresis emerges in the decomposed 2D perovskite devices (Figure S12), which is in agreement with the above-proposed decomposition-induced defect enriching mechanism. From the same consideration, PEA_2PbI_4 thin film-based device also shows slight hysteresis, whereas devices of $PEA_2PbI_4{\cdot}(MAPbI_3)_{n-1}$ (n = 2, 3) thin films show large hysteresis (Figure S12). It is worth mentioning that under all circumstances, n = 1, 2D

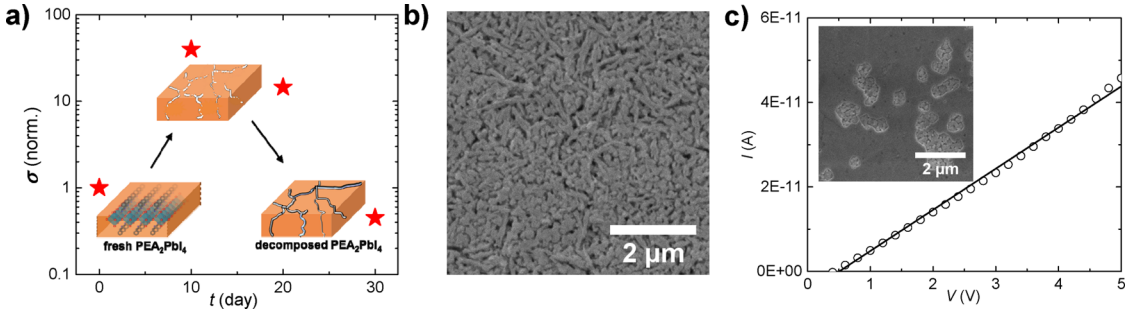

Figure 4. (a) Conductivity evolution of PEA_2PbI_4 single crystals stored in ambient conditions. The inset illustration describes the mechanism of this conductivity evolution (the crystal is shown in orange while the black part at the fracture boundaries represents insulating decomposition products). (b) SEM image of 2D perovskite single crystal surface after decomposition, showing porous morphology. (c) $I-V$ curve of n = 1 2D perovskite thin film using the device structure of Figure 2a. The inset is the corresponding SEM image of the thin film.

DOI: 10.1021/acs.nanolett.7b01475
Nano Lett. XXXX, XXX, XXX−XXX

perovskite has shown the least hysteresis in all cases, which supports the theory of mobile MA-dominant hysteresis characteristic.[27] The correspondence of the hysteresis behavior and the conductivity variation clearly supports that shallow defects in hybrid perovskites play as unintentional self-dopants, and that the gap in the shallow defect density of 3D and 2D perovskites leads to their conductivity disparity.

As a summary of the above-presented results, a positive correlation between the defect density and the conductivity is clear. Here it is worth to note that although we cannot distinguish the different defect species and characterize their densities yet, it is still reasonable to assume that an increase in the overall defect density will enrich the shallow defects, i.e., potential dopants, to contribute free carriers. Therefore, the observed sharp contrast between the conductivities of 2D and 3D perovskites can be probably traced to a defect-suppressing crystallization mechanism of 2D perovskites. Specifically, according to previous defect formation energy calculation in $MAPbI_3$, both the shallow donor defect, interstitial MA^+, and the shallow acceptor defect, MA^+ vacancy, were shown to be two of the dominant dopants with small formation energies, possibly a result of the weak interaction between MA^+ and the Pb−I framework.[2,30,31] We propose that these defects, originating from the organic cations, can be effectively suppressed in $PEA_2PbI_4{\cdot}(MAPbI_3)_{n-1}$ due to the larger steric hindrance and molecular mass of PEA compared with MA. Furthermore, the formation of iodide-related defects can be also affected due to its hydrogen bonding with the organic cation. Another plausible and more interesting explanation lies in the organic−inorganic self-assembly nature of hybrid perovskite crystallization process, which can be effectively controlled by choosing organic cations.[32] Introducing large organic cations in the hybrid perovskite system may lead to the growth of higher-quality crystals and reduction of overall defect densities. To verify this hypothesis, an in-depth study of characterizing the densities of various defect species is required, which is beyond the scope of the current Letter. Indeed, Herz's group also deduced the reduction of defect densities in $PEA_2PbI_4{\cdot}(MAPbI_3)_{n-1}$ ($n \geq 1$) compared to $MAPbI_3$ from the observation of improved carrier effective mobility in $PEA_2PbI_4{\cdot}(MAPbI_3)_{n-1}$.[22]

A direct consequence of the low dark current in $PEA_2PbI_4{\cdot}(MAPbI_3)_{n-1}$ is that electronic noise such as Nyquist noise and shot noise can be reduced accordingly.[8] Noise is unwanted random disturbance of a useful information signal in an electronic communication system. An important example is a photodetector in which the electronic noise level directly determines its light detectivity, namely, the ability of resolving weak light signals. As a demonstration, we carried out preliminary characterization of the $PEA_2PbI_4{\cdot}(MAPbI_3)_{n-1}$ crystals for photodetection.

We first measure the photoresponse of $PEA_2PbI_4{\cdot}(MAPbI_3)_{n-1}$ ($n = 1, 2, 3$) using the simple device structure as illustrated in Figure 2a. Impressive photocurrent on/off ratios exceeding 10^4 (white light, 0.1 mW cm^{-2}) are measured in 2D hybrid perovskites, in comparison with merely ~30 for both $MAPbI_3$ and $MAPbBr_3$ (Figure 5a). Despite smaller photocurrents in the 2D perovskites, their larger on−off current ratios should be advantageous for high-detectivity photodetection. The photoresponsivity spectra of the 2D perovskites are shown in Figure 5b, which match their corresponding absorption spectra. Incident light intensity (P_{light})-dependent photocurrent (I_{photo}) of the devices at the wavelength of 500 nm are presented in Figure 5c. All the $I_{photo}-P_{light}$ curves show a power law relation: $I_{photo} \propto P_{light}^{0.85}$ at low light intensity; and $I_{photo} \propto P_{light}^{0.52}$ at higher intensity. The dependence of photocurrent on incident light intensity is determined by carrier recombination mechanisms in the device.[33] The decrease of α at high P_{light} in the relation of $I_{photo} \propto P_{light}^{\alpha}$ suggests the emergence of many-body recombination, possibly exciton−exciton interaction.[34] In addition, limited charge transport across perovskite layers hinders the collection of charge carriers that are generated deep in the crystal, thus contributing to the decrease of α as well. According to the

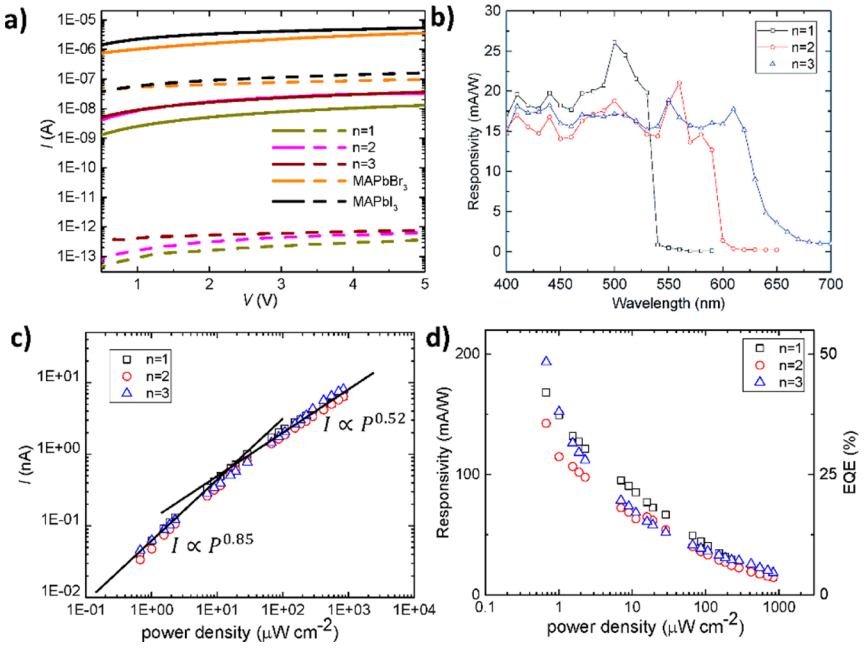

Figure 5. (a) Dark (dashed line) and illuminated (solid line, approximately 0.1 mW cm^{-2} white microscope light) $I-V$ curves of $PEA_2PbI_4{\cdot}(MAPbI_3)_{n-1}$ (n = 1, 2, 3), $MAPbI_3$, and $MAPbBr_3$. (b) Wavelength-dependent photoresponsivity spectra of $PEA_2PbI_4{\cdot}(MAPbI_3)_{n-1}$ (n = 1, 2, 3) at a fixed illumination intensity of 0.1 mW cm^{-2} and a bias of 5 V. (c) Illumination intensity-dependent photocurrent curves of the three single crystal devices at an illumination wavelength of 500 nm and a bias of 5 V, and (d) their corresponding photoresponsivity and EQE.

DOI: 10.1021/acs.nanolett.7b01475
Nano Lett. XXXX, XXX, XXX−XXX

$I_{photo}-P_{light}$ data, we can calculate the photoresponsivity R_{ph} ($R_{ph} = (I_{photo} - I_{dark})/P_{light}$) and the external quantum efficiency (EQE = $1240R_{ph}/\lambda$, λ is wavelength in nanometer), which are shown in Figure 5d. Due to the sublinear relation of $I_{photo}-P_{light}$, R_{ph} keeps rising until the lowest-achievable P_{light}, reaching over 0.15 A/W (corresponding to 37.5% EQE) for all the three devices. Higher responsivity is expectable for even weaker illumination according to the trend. We notice that the responsivity is much lower than previously reported in-plane photoconductors based on 3D perovskites.[35,36] The photoresponsivity of a photoconductor is determined by the transit time ($\tau_{transit}$) and the lifetime (τ_{life}) of photocarriers following $G = \tau_{life}/\tau_{transit}$ (G is gain and equal to $100{\cdot}EQE$). As a result of strong quantum and dielectric confinement in $PEA_2PbI_4{\cdot}(MAPbI_3)_{n-1}$,[37,38] photogenerated electron–hole pairs are strongly bounded and have much shorter lifetimes, ~150 ps (Figure S13).[18] The lifetimes of $PEA_2PbI_4{\cdot}(MAPbI_3)_{n-1}$ are more than three orders of magnitude shorter than those of 3D methylammonium lead halides and should be the major factor of restricting the photoresponsivity.

Two major types of electronic noise, shot noise, and Nyquist noise, would be reduced as a result of the low dark current in the 2D perovskites.[8] Shot noise in a photodetector is determined by the dark current following an expression: $i_{n,s} = \sqrt{2eI_dB}$, where I_d is the dark current and B is the bandwidth. Nyquist noise, or the so-called thermal noise, is determined by the resistivity and can be expressed as $i_{n,t} = \sqrt{4kTB/R}$, where R is resistivity. The total noise can be then calculated from $i_n = \sqrt{{i_{n,s}}^2 + {i_{n,t}}^2}$. A low noise level is critical for a photodetector to resolve weak signals from noise and thus to gain a high specific detectivity D^*, which is calculated from $D^* = \sqrt{AB}\,R_{ph}/i_n$, where A is the device area. The calculated D^* reaches 1.1×10^{13}, 7.2×10^{12}, and 8.6×10^{12} Jones for $n = 1$, 2, 3, respectively. These values are comparable to the highest reported so far for hybrid perovskite photoconductors.[8,35]

In summary, we revealed much lower unintentional self-doping concentrations (over three orders of magnitude) with a smaller activation energy in $PEA_2PbI_4{\cdot}(MAPbI_3)_{n-1}$ compared to 3D methylammonium lead halide. These characteristics are ascribed to a large organic cation-mediated defect-suppressing crystallization mechanism. This crystallization mechanism will benefit the design and optimization of perovskite solar cells by facilitating charge extraction and suppress hysteresis, which stands for another advantage of 2D perovskites besides stability in photovoltaic applications.[39–45] Yet, phase separation in high-n 2D perovskite thin film fabrication needs to be overcome for practical applications. The low self-doping concentration in 2D perovskites is also significant in evoking emerging optoelectronic applications that require ultralow electronic noise. Based on $PEA_2PbI_4{\cdot}(MAPbI_3)_{n-1}$ single crystals, prototypical photoconductors with distinct specific detectivity were demonstrated, suggesting their great potential for high-precision, low-power optoelectronic devices.

Experimental Methods. *Chemicals.* Methylammonium iodide were purchased from Dyesol (Australia). All the other chemicals and solvents were purchased from Sigma-Aldrich and met ACS reagent grade.

Synthesis. $PEA_2PbI_4{\cdot}(MAPbI_3)_{n-1}$ ($n = 1, 2, 3$) single crystals were grown using a previously reported cooling method. Briefly, precursors containing lead oxide, methylammonium iodide, and phenethylamine with specific ratios were dissolved in hydriodic acid (HI) solution (57% *w/w* in water) at ~90 °C. The solution was then slowly cooled to room temperature at a rate of 1 °C/h. The ratios are 1.72/0/3.45 mmol, 6/18/1 mmol, and 10/24/1 mmol for $n = 1$, 2, 3, respectively, in 30 mL of HI solution. It is worth noting that larger n-members ($n > 3$) of this 2D perovskite family can be also grown but in a mixture form, which should be caused by a large solubility difference between PEA and MA in the aqueous solution. $MAPbI_3$ and $MAPbBr_3$ single crystals were grown as previously reported.[46] As-grown crystals were rinsed with diethyl ether and then dried under vacuum.

Device Fabrication. All the 2D perovskite single crystal-based devices were fabricated by simply thermally evaporating 60 nm-thick Au electrodes on the freshly exfoliated crystal surface with specific metal masks (patterns and dimensions were illustrated in the main text). The crystals were attached onto glass substrates with double-side tape and then exfoliated by using the tip of a blade to pry the crystal edge. For 3D perovskite devices, gold electrodes were directly deposited on the fresh crystals. For four-point probe measurement, the 3D perovskite single crystals were polished down to 200 μm using a M-Prep 6 manual polisher (Allied High Tech Products, Inc., USA) with silicon carbide papers (600 grit to 60 grit). Two-dimensional perovskite thin films were deposited by simply spin-coating 0.5 M stoichiometric solution in DMF on glass substrates. The thin film devices were also fabricated by thermally evaporating Au electrodes on the surface.

Characterization. XRD was carried out with a Bruker D8 Advance using a Cu $K_{\alpha 1}$ (λ = 1.5406 Å) source, a step size of 0.02°, and a speed of 0.5 s/step. The absorption spectra were captured by measuring the diffuse reflectance spectra of crystal powders using a Cary 5000 (Agilent Technologies). The sample for diffuse reflectance measurement was prepared by mixing the crystal powders with freshly dried KBr powders in a weight ratio of 1:100. The PL spectra were collected using an Aramis Raman Spectroscopy (Horiba Scientific, USA) with a 473 nm laser. Time-resolved PL spectra were captured with a high-resolution streak camera (Hamamatsu C10910). SEM images were captured with a Quanta-600 (FEI). Optical microscopy images were acquired with an Olympus BX61 microscope. $I-V$ measurements were carried out in a CPS-196 cryogenic probe station (TPS Inc., Taiwan) with a Keithley 4200 equipped with remote preamplifiers. To measure the extremely low dark current, a large delay factor and filter factor were used to ensure stabilization and low noise of measured current. For photoresponsivity measurement, a xenon light source (350–700 nm) was used. The intensity was controlled through varying the power of the lamp and neutral density filters, and was calibrated with a power meter. For temperature-dependent measurement, the temperature was controlled through a Lake Shore 336 temperature controller with liquid nitrogen.

DFT Calculation. Crystal structure optimizations and electronic band calculations were performed using DFT implemented in the PWSCF code of the Quantum ESPRESSO package.[47] The exchange-correlation energy was approximated using the generalized gradient approximation (GGA) proposed by Perdew–Burke–Ernzerhof (PBE). Electron–ion interactions were described by ultrasoft pseudopotentials including scalar-relativistic or full-relativistic effects through explicitly treating electrons for H ($1s^1$), N, and C ($2s^2$, $2p^2$), I ($5s^2$, $5p^2$), and Pb ($5d^{10}$, $6s^2$, $6p^2$). Single-particle wave functions (charges) were expanded on a plane-wave basis set up to a kinetic energy cutoff of 50 Ry (300 Ry) for all hybrid perovskites. Monkhorst–Pack type K-meshes of $6 \times 6 \times 6$ for the tetragonal-phase $MAPbI_3$ and

DOI: 10.1021/acs.nanolett.7b01475
Nano Lett. XXXX, XXX, XXX–XXX

$6 \times 6 \times 2$ for $PEA_2PbI_4{\cdot}(MAPbI_3)_{n-1}$ (n = 1, 2, 3). The crystal structures were fully relaxed until the total force on each atom was less than 0.01 eV/Å. The effective masses for both electron and hole were calculated by fitting of the dispersion relation of $m = \hbar\left[\frac{\partial^2 E(k)}{\partial k^2}\right]^{-1}$ from electronic bands along the direction Γ−F; and the deformation potential was estimated by the equation of $E_1 = \frac{\Delta E_{CBM/VBM}}{\Delta V / V_0}$.

■ ASSOCIATED CONTENT

Supporting Information

The Supporting Information is available free of charge on the ACS Publications website at DOI: 10.1021/acs.nanolett.7b01475.

Additional photographic images of crystals, XRD patterns, $I-V$ curves, band structures, projected density of states, a supporting table of calculated effective masses and lattice deformation potentials, simulated temperature dependence of conductivity, optic microscopic and SEM images, PL spectra, and time-resolved PL spectra (PDF)

■ AUTHOR INFORMATION

Corresponding Author

*E-mail: osman.bakr@kaust.edu.sa.

ORCID

Olivier Ouellette: 0000-0001-5708-5058
Banavoth Murali: 0000-0002-7806-2274
Chao Shen: 0000-0003-2860-8897
Jr-Hau He: 0000-0003-1886-9241
Omar F. Mohammed: 0000-0001-8500-1130
Osman M. Bakr: 0000-0002-3428-1002

Present Address

[#]School of Chemistry, University of Hyderabad, Hyderabad, India.

Notes

The authors declare no competing financial interest.

■ ACKNOWLEDGMENTS

Financial support for this work was provided by KAUST. W.P. would like to acknowledge Chun Ma at KAUST for his valuable suggestions on the measurement of photodetector noise, and Feng Li and Ting-You Li at KAUST for their assistance in measuring temperature-dependent conductivity.

■ REFERENCES

(1) Koenraad, P. M.; Flatte, M. E. *Nat. Mater.* **2011**, *10*, 91−100.
(2) Ball, J. M.; Petrozza, A. *Nat. Energy* **2016**, *1*, 16149.
(3) Li, W.; Wang, Z.; Deschler, F.; Gao, S.; Friend, R. H.; Cheetham, A. K. *Nat. Rev. Mater.* **2017**, *2*, 16099.
(4) Wang, Q.; Shao, Y.; Xie, H.; Lyu, L.; Liu, X.; Gao, Y.; Huang, J. *Appl. Phys. Lett.* **2014**, *105*, 163508.
(5) Guerrero, A.; Juarez-Perez, E. J.; Bisquert, J.; Mora-Sero, I.; Garcia-Belmonte, G. *Appl. Phys. Lett.* **2014**, *105*, 133902.
(6) Edri, E.; Kirmayer, S.; Mukhopadhyay, S.; Gartsman, K.; Hodes, G.; Cahen, D. *Nat. Commun.* **2014**, *5*, 3461.
(7) Peng, W.; Wang, L.; Murali, B.; Ho, K.-T.; Bera, A.; Cho, N.; Kang, C.-F.; Burlakov, V. M.; Pan, J.; Sinatra, L.; Ma, C.; Xu, W.; Shi, D.; Alarousu, E.; Goriely, A.; He, J.-H.; Mohammed, O. F.; Wu, T.; Bakr, O. M. *Adv. Mater.* **2016**, *28*, 3383−3390.
(8) Fang, Y.; Huang, J. *Adv. Mater.* **2015**, *27*, 2804−2810.
(9) García de Arquer, F. P.; Armin, A.; Meredith, P.; Sargent, E. H. *Nat. Rev. Mater.* **2017**, *2*, 16100.
(10) Stoumpos, C. C.; Cao, D. H.; Clark, D. J.; Young, J.; Rondinelli, J. M.; Jang, J. I.; Hupp, J. T.; Kanatzidis, M. G. *Chem. Mater.* **2016**, *28*, 2852−2867.
(11) Calabrese, J.; Jones, N. L.; Harlow, R. L.; Herron, N.; Thorn, D. L.; Wang, Y. *J. Am. Chem. Soc.* **1991**, *113*, 2328−2330.
(12) Pedesseau, L.; Sapori, D.; Traore, B.; Robles, R.; Fang, H.-H.; Loi, M. A.; Tsai, H.; Nie, W.; Blancon, J.-C.; Neukirch, A.; Tretiak, S.; Mohite, A. D.; Katan, C.; Even, J.; Kepenekian, M. *ACS Nano* **2016**, *10*, 9776−9786.
(13) Miccoli, I.; Edler, F.; Pfnür, H.; Tegenkamp, C. *J. Phys.: Condens. Matter* **2015**, *27*, 223201.
(14) Jones, E. D., Control of Semiconductor Conductivity by Doping. In *Electronic Materials: From Silicon to Organics*; Miller, L. S., Mullin, J. B., Eds.; Springer US: Boston, MA, 1991; pp 155−171.
(15) Zhu, H.; Miyata, K.; Fu, Y.; Wang, J.; Joshi, P. P.; Niesner, D.; Williams, K. W.; Jin, S.; Zhu, X.-Y. *Science* **2016**, *353*, 1409−1413.
(16) Mante, P.-A.; Stoumpos, C. C.; Kanatzidis, M. G.; Yartsev, A. *Nat. Commun.* **2017**, *8*, 14398.
(17) Guo, Z.; Wu, X.; Zhu, T.; Zhu, X.; Huang, L. *ACS Nano* **2016**, *10*, 9992−9998.
(18) Wu, X.; Trinh, M. T.; Niesner, D.; Zhu, H.; Norman, Z.; Owen, J. S.; Yaffe, O.; Kudisch, B. J.; Zhu, X. Y. *J. Am. Chem. Soc.* **2015**, *137*, 2089−2096.
(19) Li, X.; Mullen, J. T.; Jin, Z.; Borysenko, K. M.; Nardelli, M. B.; Kim, K. W. *Phys. Rev. B: Condens. Matter Mater. Phys.* **2013**, *87*, 115418.
(20) Mitzi, D. B.; Dimitrakopoulos, C. D.; Rosner, J.; Medeiros, D. R.; Xu, Z.; Noyan, C. *Adv. Mater.* **2002**, *14*, 1772−1776.
(21) Li, F.; Ma, C.; Wang, H.; Hu, W.; Yu, W.; Sheikh, A. D.; Wu, T. *Nat. Commun.* **2015**, *6*, 8238.
(22) Milot, R. L.; Sutton, R. J.; Eperon, G. E.; Haghighirad, A. A.; Martinez Hardigree, J.; Miranda, L.; Snaith, H. J.; Johnston, M. B.; Herz, L. M. *Nano Lett.* **2016**, *16*, 7001−7007.
(23) Johnston, M. B.; Herz, L. M. *Acc. Chem. Res.* **2016**, *49*, 146−154.
(24) Pierret, R. F. *Semiconductor Device Fundamentals*; Addison-Wesley: 1996.
(25) Adinolfi, V.; Yuan, M.; Comin, R.; Thibau, E. S.; Shi, D.; Saidaminov, M. I.; Kanjanaboos, P.; Kopilovic, D.; Hoogland, S.; Lu, Z.-H.; Bakr, O. M.; Sargent, E. H. *Adv. Mater.* **2016**, *28*, 3406−3410.
(26) Peng, W.; Miao, X.; Adinolfi, V.; Alarousu, E.; El Tall, O.; Emwas, A.-H.; Zhao, C.; Walters, G.; Liu, J.; Ouellette, O.; Pan, J.; Murali, B.; Sargent, E. H.; Mohammed, O. F.; Bakr, O. M. *Angew. Chem., Int. Ed.* **2016**, *55*, 10686−10690.
(27) Yuan, Y.; Chae, J.; Shao, Y.; Wang, Q.; Xiao, Z.; Centrone, A.; Huang, J. *Adv. Energy Mater.* **2015**, *5*, 1500615.
(28) Azpiroz, J. M.; Mosconi, E.; Bisquert, J.; De Angelis, F. *Energy Environ. Sci.* **2015**, *8*, 2118−2127.
(29) Eames, C.; Frost, J. M.; Barnes, P. R. F.; O'Regan, B. C.; Walsh, A.; Islam, M. S. *Nat. Commun.* **2015**, *6*, 7497.
(30) Buin, A.; Pietsch, P.; Xu, J.; Voznyy, O.; Ip, A. H.; Comin, R.; Sargent, E. H. *Nano Lett.* **2014**, *14*, 6281−6286.
(31) Yin, W.-J.; Shi, T.; Yan, Y. *Appl. Phys. Lett.* **2014**, *104*, 063903.
(32) Mitzi, D. B. *J. Chem. Soc., Dalton Trans.* **2001**, 1−12.
(33) Heilmeier, G. H.; Harrison, S. E. *J. Appl. Phys.* **1963**, *34*, 2732−2735.
(34) Choi, S. i.; Rice, S. A. *J. Chem. Phys.* **1963**, *38*, 366−373.
(35) Saidaminov, M. I.; Adinolfi, V.; Comin, R.; Abdelhady, A. L.; Peng, W.; Dursun, I.; Yuan, M.; Hoogland, S.; Sargent, E. H.; Bakr, O. M. *Nat. Commun.* **2015**, *6*, 8724.
(36) Fang, H.; Li, Q.; Ding, J.; Li, N.; Tian, H.; Zhang, L.; Ren, T.; Dai, J.; Wang, L.; Yan, Q. *J. Mater. Chem. C* **2016**, *4*, 630−636.
(37) Hong, X.; Ishihara, T.; Nurmikko, A. V. *Phys. Rev. B: Condens. Matter Mater. Phys.* **1992**, *45*, 6961−6964.
(38) Papavassiliou, G. C. *Prog. Solid State Chem.* **1997**, *25*, 125−270.
(39) Smith, I. C.; Hoke, E. T.; Solis-Ibarra, D.; McGehee, M. D.; Karunadasa, H. I. *Angew. Chem.* **2014**, *126*, 11414−11417.
(40) Quan, L. N.; Yuan, M.; Comin, R.; Voznyy, O.; Beauregard, E. M.; Hoogland, S.; Buin, A.; Kirmani, A. R.; Zhao, K.; Amassian, A.; Kim, D. H.; Sargent, E. H. *J. Am. Chem. Soc.* **2016**, *138*, 2649−2655.

DOI: 10.1021/acs.nanolett.7b01475
Nano Lett. XXXX, XXX, XXX−XXX

(41) Tsai, H.; Nie, W.; Blancon, J.-C.; Stoumpos, C. C.; Asadpour, R.; Harutyunyan, B.; Neukirch, A. J.; Verduzco, R.; Crochet, J. J.; Tretiak, S.; Pedesseau, L.; Even, J.; Alam, M. A.; Gupta, G.; Lou, J.; Ajayan, P. M.; Bedzyk, M. J.; Kanatzidis, M. G.; Mohite, A. D. *Nature* **2016**, *536*, 312−316.
(42) Yuan, M.; Quan, L. N.; Comin, R.; Walters, G.; Sabatini, R.; Voznyy, O.; Hoogland, S.; Zhao, Y.; Beauregard, E. M.; Kanjanaboos, P.; Lu, Z.; Kim, D. H.; Sargent, E. H. *Nat. Nanotechnol.* **2016**, *11*, 872−877.
(43) Blancon, J.-C.; Tsai, H.; Nie, W.; Stoumpos, C. C.; Pedesseau, L.; Katan, C.; Kepenekian, M.; Soe, C. M. M.; Appavoo, K.; Sfeir, M. Y.; Tretiak, S.; Ajayan, P. M.; Kanatzidis, M. G.; Even, J.; Crochet, J. J.; Mohite, A. D. *Science* **2017**, *355*, 1288.
(44) Byun, J.; Cho, H.; Wolf, C.; Jang, M.; Sadhanala, A.; Friend, R. H.; Yang, H.; Lee, T.-W. *Adv. Mater.* **2016**, *28*, 7515−7520.
(45) Kim, Y.-H.; Cho, H.; Lee, T.-W. *Proc. Natl. Acad. Sci. U. S. A.* **2016**, *113*, 11694−11702.
(46) Saidaminov, M. I.; Abdelhady, A. L.; Murali, B.; Alarousu, E.; Burlakov, V. M.; Peng, W.; Dursun, I.; Wang, L.; He, Y.; Maculan, G.; Goriely, A.; Wu, T.; Mohammed, O. F.; Bakr, O. M. *Nat. Commun.* **2015**, *6*, 7586.
(47) Giannozzi, P.; Baroni, S.; Bonini, N.; Calandra, R.; Car, C.; Cavazzoni, C.; Ceresoli, D.; Chiarotti, G. L.; Cococcioni, M.; Dabo, I.; et al. *J. Phys.: Condens. Matter* **2009**, *21*, 395502.

DOI: 10.1021/acs.nanolett.7b01475
Nano Lett. XXXX, XXX, XXX−XXX